This is the accepted manuscript made available via CHORUS. The article has been published as:

Structural and magnetic transitions in spinel FeMn_{2}O_{4} single crystals

Roshan Nepal, Qiang Zhang, Samuel Dai, Wei Tian, S. E. Nagler, and Rongying Jin

Phys. Rev. B **97**, 024410 — Published 11 January 2018

DOI: 10.1103/PhysRevB.97.024410

Structural and Magnetic Transitions in Spinel $FeMn_2O_4$ Single Crystals

Roshan Nepal[1], Qiang Zhang[1], Samuel Dai[1], Wei Tian[2], S. E. Nagler[2], Rongying Jin[1,*]

[1]Department of Physics and Astronomy, Louisiana State University, Baton Rouge, LA 70803

[2]Quantum Condensed Matter Division, Oak Ridge National Laboratory, Oak Ridge, TN 37831

Abstract

Materials that form the spinel structure are known to exhibit geometric frustration, which can lead to magnetic frustration as well. Through magnetization and neutron diffraction measurements, we find that $FeMn_2O_4$ undergoes one structural and two magnetic transitions. The structural transition occurs at $T_s \sim 595$ K from cubic at high temperatures to tetragonal at low temperatures. Two magnetic transitions are ferrimagnetic at $T_{FI-1} \sim 373$ K and $T_{FI-2} \sim 50$ K, respectively. Further investigation of the specific heat, thermal conductivity, and Seebeck coefficient confirms both magnetic transitions. Of particular interest is that there is a significant magnetic contribution to the low-temperature specific heat and thermal conductivity, providing a unique system to study heat transport by magnetic excitations.

* Email address: rjin@lsu.edu

Introduction

Spinel oxides are of great importance in basic science and potential applications due to their wide range of exciting magnetic properties such as frustrated antiferromagnetism, multiferroics, spintronics, spin-orbital liquids, and orbital glass behavior [1–6]. These are derived from their unique structure with general chemical formula AB_2O_4, where A and B are usually transition metals. The ionic distribution of spinels is often written as $(A_{1-\alpha}B_{\alpha})[A_{\alpha}B_{2-\alpha}]O_4$, with the elements in the parenthesis and the square brackets residing in the tetrahedra and the octahedra formed by the oxygen ions, respectively [5,6]. Here, α represents the *degree of inversion*, variable between 0 and 1 [7,8]. If $\alpha = 0$, it is regarded as normal spinel structure with A in the tetrahedral and B in the octahedral environment. If $\alpha = 1$, an inverse spinel structure is formed with half of the B atoms and all of A atoms in the octahedra, while the remaining B atoms in the tetrahedra. The structures with $0 < \alpha < 1$ are known as mixed spinels where A and B atoms partially residing in both tetrahedral and octahedral environment.

If A and B are magnetic elements, the spinel compounds may be considered as two sets of magnetic sublattices: one with ions residing in the tetrahedra (T sublattice) and the other in octahedra (O sublattice) [9]. While the T subliattice forms the diamond-like structure not frustrated for nearest-neighbor interactions, the O sublattice is pyrochlore-like giving rise to frustrated magnetic interactions. Typically, the ions within a sublattice interact ferromagnetically (FM) whereas the ions between two sublattices interact antiferromagnetically (AFM) [8,9]. According to Neel theory [9], the exchange interaction between the ions of T and O sublattices is much stronger than the exchange interaction within the sublattice. Due to the unequal numbers of T and O sites and the dominating interaction between two sublattices, a net magnetic moment is developed, in favor of ferrimagnetic (FI) ordering [8–10].

$Mn_xFe_{3-x}O_4$ is one of the earliest studied spinel oxides [11–13]. At room temperature, it crystallizes in a cubic structure for $x < 2$, or in a tetragonal structure for $x \geq 2$ [12]. The tetragonal structure is manifested due to a cooperative Jahn-Teller (JT) distortion of the MnO_6 octahedra [12–14]. Magnetically, this system orders in a ferrimagnetic (FI) configuration [15,16]. While there is a trend that the transition temperature T_{FI} decreases with increasing x [17], most of these studies have been on the iron-rich region i.e. $x < 1$. To date, there are few reports on the manganese-rich compounds [15,18–20]. Figure 1(a) shows the crystal structure of $FeMn_2O_4$ ($x = 2$), where all Fe ions occupy the octahedral site along with Mn ions. In other words, it forms an inverse spinel structure with $\alpha = 1$ [17,21]. Here, we report, for the first time, the structural (neutron powder diffraction), magnetic (magnetization), and thermal properties (specific heat, thermal conductivity, and thermopower) of $FeMn_2O_4$ single crystals. One structural transition and two magnetic transitions are identified via magnetization and neutron diffraction measurements. At low temperatures, magnetic excitations have significant impact on thermal properties including thermal conductivity and specific heat.

EXPERIMENTAL PROCEDURE

Single crystalline $FeMn_2O_4$ was grown using a two-mirror optical floating zone furnace. For the growth, we first synthesized polycrystalline $FeMn_2O_4$ via the solid - state reaction of the mixture of Fe_2O_3 and Mn_2O_3 with an 1 : 2 molar ratio. It was heated at 1250°C for 12 hours, and quenched in liquid nitrogen in order to obtain the spinel structure. The quenched sample was re-ground and annealed in air at 200°C for 5 days to get rid of the high-temperature cubic phase. The polycrystalline sample was then hydrostatically pressed into rods, and further sintered at 1250°C for 12 hours. The growth rate of 3 mm/h was used while the upper and bottom rods were rotated in opposite directions at 30 rpm to minimize inhomogeneity.

The phase purity of the samples was verified via powder x-ray diffraction measurements using PANalytical Empyrean x-ray diffractometer (Cu Kα radiation) and neutron Laue diffraction. The chemical compositions of the single crystals were measured using Energy Dispersive X-ray Spectroscopy (EDS) equipped by FEI Wuanta 200 under the vacuum environment. The low-temperature (2 K to 400 K) magnetization measurements were performed in a Magnetic Properties Measurement System (MPMS – 7 T, *Quantum Design*), and the high-temperature (300 K to 1000 K) magnetization measurements were performed using the Vibrating Sample Magnetometer (VSM) in a Physical Properties Measurement System (PPMS – 14 T, *Quantum Design*). The temperature dependence of specific heat, thermal conductivity, and thermopower was measured using the PPMS between 2 and 400 K. For four-probe electrical resistivity measurements, we utilized a Keithley 2601A SYSTEM SourceMeter®, along with the PPMS for variable temperatures. Neutron powder diffraction measurements (between room temperature and 700 K) were performed using the HB-1A triple-axis spectrometer at the High Flux Isotope Reactor, Oak Ridge National Laboratory.

RESULTS AND DISCUSSION

A typical single crystal boule obtained from the floating-zone furnace is shown in the inset of Figure 1(b). The room-temperature x-ray diffraction data obtained from powder made by crushing single crystals is shown in the main panel of Figure 1(b). All peaks can be indexed under a tetragonal crystal structure ($I4_1/amd$, No. 141) with $a = b = 5.91$ Å and $c = 8.91$ Å, indicating a single phase. The lattice parameters of such structure are usually reported in pseudo-cubic notation. In this notation, the lattice parameters are transformed to $a' = \sqrt{2}a = 8.36$ Å and $c' = c = 8.91$ Å with $c'/a' = 1.07$ [22], which is comparable with the previous reports [15,20]. Interestingly, neutron diffraction indicates that single crystal grows along the $(111)_C$ direction, as illustrated in the inset of Figure 1(b). This suggests that chemical bond is the strongest along the $(111)_C$ direction. From the EDS measurements we found that the actual Fe : Mn ratio was indeed 1 : 2 in our single crystal, indicating the correct spinel phase.

Our neutron powder diffraction measurement confirms the pseudo-cubic (tetragonal) structure at room temperature. Figure 1(c) shows the neutron diffraction pattern in the range of $96^\circ < 2\theta < 118^\circ$ (wave length $\lambda = 2.36$ Å) at three different temperatures. The peaks are labeled in pseudo-cubic notation and the peak at $2\theta \sim 111^\circ$ can be indexed as aluminum (220) reflection from the aluminum sample holder. It can be seen that, at 423 K (blue dots), both $(440)_C$ and $(404)_C$ peaks are present and well separated. At 583 K (green dots), the two peaks seem to move toward each other with decreased intensities. At an even higher temperature of 618 K (red dots), the $(440)_C$ and $(404)_C$ peaks merge into a single peak, indicating a structural transition between 583 K and 618 K in $FeMn_2O_4$. The crystal structure becomes cubic at high temperatures. In order to determine the transition temperature, we traced the $(404)_C$ peak as a function of temperature. Figure 1(d) shows the temperature dependence of the $(404)_C$ integrated intensity. It shows that the $(404)_C$ peak becomes detectable below 618 K. The scattering intensity increases with decreasing temperature and tends to saturate below 550 K. This suggests that the cubic-tetragonal transition has a transition temperature window of $\Delta T_s \sim 618 - 550 = 68$ K. We thus determine the transition temperature $T_s \sim 595$ K, corresponding to the peak position in the derivative of intensity with respect to temperature (see the inset of Figure 1(d)). This transition temperature is much higher than that obtained from thermal expansion measurement [19]. However, it was also reported that the structural transition occurs near 623 K for $Fe_{0.9}Mn_{2.1}O_4$ ($x = 2.1$) [19]. This suggests that the structural transition is intimately connected to Mn concentration and distribution as discussed previously [10].

Figure 2(a) shows the temperature dependence of the magnetization (M) between 2 and 800 K measured by applying 1000 Oe field along the $(111)_C$ direction of $FeMn_2O_4$. Black open circles represent the zero-field-cooling (ZFC) and field-cooling (FC) magnetization data obtained from SQUID (MPMS), while red circles represent the data from VSM. A good agreement can be seen between the two sets of data in the overlapping region between 300 K and 400 K. Interestingly, there is no anomaly near the structure transition region (see the inset of Fig. 2(a)). Instead, we note the sharp raise of M below ~ 400 K, and an obvious decrease below 50 K. For the easy determination of the transition temperatures, we calculate dM/dT as shown in Figure 2(b). Note that there are two peaks with one at T_{FI-1} ~ 373 K and the other at T_{FI-2} ~ 50 K. The transition temperatures are comparable to those previously reported [11,15]. In a previous neutron diffraction study, the authors reported a ferrimagnetic ordering below 390 K followed by sublattice spin reorientations below 55 K resulting in a non-collinear ordering [15]. The downturn in M(T) below T_{FI-2} indicates the reduced net magnetic moment, consistent with the non-collinear behavior. Applying magnetic field perpendicular to the $(111)_C$ direction yields similar magnetic behavior, with small difference in saturation moment as shown in the inset of Fig. 2(b). This indicates that the magnetic easy axis is also along the $(111)_C$ direction.

To further understand the nature of these magnetization anomalies, we analyze the high-temperature susceptibility χ = M/H using a modified Curie-Weiss formula,

$$\chi = \chi_0 + \frac{C}{T-\theta}. \qquad (1)$$

Here, χ_0 describes the temperature-independent contribution, θ is the Curie-Weiss temperature and C is the Curie constant. By fitting our paramagnetic susceptibility data up to T_s to Eq. (1), we obtain χ_0 = 0.00776 emu/mol, C = 0.259 emu-K/mol, and θ = 393 K. Figure 2(c) displays $1/\chi$

as a function of temperature between 350 K and 600 K, and the fitting curve (green). While Eq. (1) fits our data reasonably well between 450 K and 600 K and the value of θ is close to T_{FI-1}, χ_0 is high, and C is considerably small. In view of field dependence of magnetization at high temperatures as shown in Fig. 2(d), it is simply linear behavior above 420 K. This indicates that large χ_0 is unlikely due to ferromagnetic-like impurity. On the other hand, from $C = N_A \mu_{eff}^2 / 3k_B$ (N_A is the Avogadro constant and k_B is the Boltzmann constant), we obtain the effective magnetic moment ~ 1.44μ_B/f.u.. According to Ref. [15], the magnetic moment is ~ 4.3μ_B for the T sublattice, and ~ 3.1μ_B for the O sublattice. This indicates that the ferrimagnetic interaction cannot be described by the simple Curie-Weiss law. According to the molecular field theory of ferrimagnetism, the susceptibility above the transition temperature is better characterized by the Neel's expression [9,16],

$$\frac{1}{\chi} = \frac{T - \theta_a}{C'} - \frac{\xi}{T - \theta'}. \qquad (2)$$

Here, the first term describes the high-T asymptotic behavior, and the second term describes the hyperbolic behavior near the ferrimagnetic transition. The red curve in Fig. 2(c) represents the results from the fit of Eq. (2) to the experimental data between 420 K and 595 K with θ_a = -824 K, C' = 11.91 emu-K/mol, θ' = 389.9 K, and ξ = 1495 mol-K/emu.

In Eq. (2), θ_a, C', θ', and ξ are fitting parameters derived from the two-sublattice model of ferrimagnetism [9,16]. The parameter θ_a, known as the asymptotic Curie temperature, measures the strength of antiferromagnetic exchange coupling of spins between the two sublattices [23,24]. The large value of θ_a with the ratio $|\theta_a|/T_{FI-1} \approx 2.6 > 1$ suggests an appreciable magnetic frustration in the system [25]. The characteristic temperature θ' should be close to the ferrimagnetic transition temperature [26], which is seen in our case. The parameter *C'* is the sum of the sublattice Curie constants, i.e. $C' = C_T + C_O$ [9,16,23], which allows us to estimate the effective magnetic moment ~ $9.76\mu_B$ per formula. Assuming the cation distribution is $(Mn^{2+})_T[Fe^{3+}Mn^{3+}]_OO_4$, we can calculate the theoretical magnetic moment $5.9\mu_B/Mn^{2+}$ (S = 5/2: the high spin state) in the tetrahedral environment, and ~ $4.9\mu_B/Mn^{3+}$ (S = 2: the high spin state) and $5.9\mu_B/Fe^{3+}$ (S = 5/2: the high spin state) in the octahedral environments [16]. Using $\mu_{eff}^2 = \mu_O^2 + \mu_T^2$ [24,27], the theoretical effective moment is μ_{eff} ~ $9.68\mu_B$, close to our experimental value. If it is distributed as $(Mn^{2+}_{0.9}Fe^{3+}_{0.1})_T[Fe^{3+}_{0.8}Fe^{2+}_{0.1}Mn^{3+}_{1.1}]_OO_4$ as concluded previously [15,28,29], the calculated value should be even larger, i.e., closer to our experimental value. This suggests that Mn and Fe ions are in their high spin states.

To further confirm the ferrimagnetic nature below T_{FI-1}, we measured the isothermal field dependence of magnetization of $FeMn_2O_4$, which is presented in Figure 2(e). At 400 K, a non-linear M(H) develops at low fields, indicating the entrance of magnetically ordered state. Upon further cooling, the non-linear M(H) becomes more profound, forming a hysteresis loop centered at the origin and saturation out of the loop, as demonstrated in the inset of Fig. 2(e). The saturation magnetization and coercive field increase with decreasing temperature. The hysteresis loop and negative θ_a indicate that the magnetic anomaly at T_{FI-1} ~ 373 K is due to ferrimagnetic ordering which is consistent with the result obtained from previous neutron diffraction study [15].

At $T_{FI-2} < T < T_{FI-1}$, the magnetization reaches saturation easily as seen in Figure 2(e), suggesting soft ferrimagnetic nature. Below T_{FI-2}, M(H) behaves differently from that at high temperatures. As shown in Fig. 2(f), M continuously increases with increasing H without saturation up to 70 kOe down to 2 K. This implies that magnetic alignment below T_{FI-2} is more difficult than that above T_{FI-2}. In view of other spinel materials with two magnetic transitions, the transition occurring at a lower temperature is usually due to the canting of B-site spins [30,31]. It is likely the same origin for the transition at T_{FI-2} in $FeMn_2O_4$. As enlarged in the inset of Fig. 2(f), the non-collinear magnetic alignment results in larger hysteresis loop than that in the collinear situation at high temperatures. With decreasing temperature, the decrease of magnetic susceptibility (Fig. 2(a)) and the enhanced coercive field seen in hysteresis loops (Fig. 2(f)) indicate the non-collinear magnetic ground state.

Magnetic ordering usually involves entropy change, thus resulting in specific heat anomaly. The temperature dependence of the specific heat C_p of $FeMn_2O_4$ between 2 and 400 K is shown in Figure 3(a). There is clearly a peak at T_{FI-1}, indicating a true phase transition. The small peak suggests that most entropy is removed prior to ordering. Even though there is a sharp decrease in magnetization, there is no sign in specific heat at T_{FI-2}, while it tends to vary slower at low temperatures as seen in dC_p/dT (see the inset of Figure 3(a)). Nevertheless, we find the low-temperature specific heat can be described by the following equation:

$$C_p(T) = \beta \mathrm{T}^3 + \delta \mathrm{T}^{3/2} e^{-\Delta_m/T}. \qquad (3)$$

Here, the first term is the Debye phonon specific heat with $\beta = (12\pi^4/5)nN_A k_B/\theta_D{}^3$ (where θ_D is the Debye temperature and $n = 7$ for $FeMn_2O_4$). The second term is the magnetic contribution to the specific heat in a ferri- or ferro-magnetic system [32–34], with δ a constant related to the spin-wave stiffness and Δ_m the anisotropy related spin-wave gap. As shown in Figure 3(b), the behavior of specific heat below 10 K is well described by Eq. (3) with the fitting parameters $\beta = 2.2 \times 10^{-4}$ J/mol-K^4, $\delta = 0.033$ J/mol-K$^{5/2}$ and $\Delta_m = 1.03$ K. From the β value, we can estimate the Debye temperature $\theta_D \approx 395$ K, which is comparable to the previous reports on other manganese ferrites [35]. For comparison, we plot the magnetic contribution (C_{mag}) and the phonon contribution (C_{ph}) in Figure 3(b) as well. Remarkably, the magnetic contribution is much larger than the phonon contribution, indicating that heat is mostly carried by magnetic excitation. Below 10 K, C_{ph} is almost negligible. This is similar to previous observation in $MnFe_2O_4$ nanoparticles [29, to be added].

The small phonon contribution is also reflected in thermal conductivity. Figure 3(c) shows the temperature dependence of the thermal conductivity κ. Overall, the temperature profile is prototypical for crystalline materials with a broad peak around 80 K because of Umklapp scattering processes at high temperatures. On the other hand, the "tail" above ~ 250 K is likely due to the thermal radiation at high temperatures. Similar to the specific heat, no apparent anomaly is observed at T_{FI-2}, suggesting little entropy removal. *What is remarkable is the low thermal conductivity in the entire temperature range for a solid, with the maximum ~ 1.7 W/K-m.* There are several possible origins for such a low thermal conductivity: (1) geometric frustration due to the spinel structure as reflected by the high Debye temperature, (2) scattering by disorder as discussed above with both Mn and Fe partially occupying the A and B sites, and (3) magnon-phonon scattering [36,37].

We now focus on the low temperature behavior of κ. Since it is an insulator, we can write κ as a sum of phonon contribution κ_{ph} and magnetic contribution κ_{mag}, both solely depending on the specific heat at low temperatures [38,39]. Given that Eq. (3) describes well our low-temperature specific heat, one would expect two contributions to κ as well. Figure 3(d) displays κ(T) plotted as κ versus $\mathrm{T}^{3/2}e^{-\Delta_m/T}$ between 2 and 35 K using the Δ_{m} value obtained from specific heat. Below 20 K, κ clearly shows a linear dependence with $\mathrm{T}^{3/2}e^{-\Delta_m/T}$ as illustrated by the red linear fitting line. This indicates that the low-temperature κ is proportional to C_{mag}, without any sign of the contribution from phonons.

The low thermal conductivity makes crystalline $FeMn_2O_4$ promising for applications, such as thermoelectrics. The temperature dependence of Seebeck coefficient (S) of $FeMn_2O_4$ is shown in Figure 4(a). While it is negligible at temperatures below 250 K, the magnitude of negative thermopower increases with increasing temperature, reaching the maximum at the onset of ferrimagnetic transition. The negative thermopower indicates that heat is mainly carried via electrons (n-type). The downturn of S at T_{FI-1} indicates the effect of magnetic transition, which likely changes the electronic structure [40].

Large thermopower and small thermal conductivity are desired properties for thermoelectrics. Unfortunately, the electrical resistivity (ρ) of $FeMn_2O_4$ is too high, and it only becomes measurable above room temperature. Figure 4(b) shows the temperature dependence of ρ between 300 K and 400 K, which decreases exponentially with increasing temperature. With the application of a magnetic field, a negative magnetoresistance is seen, consistent with the ferrimagnetism. The temperature dependence of ρ can be modeled by the Arrhenius equation:

$$\rho(\mathrm{T}) = \rho(0)e^{\frac{\Delta}{2k_BT}}, \qquad (4)$$

where Δ is the activation energy. Our experimental data fits quite well with Eq. (4) as shown in Fig. 4(b). From the fit, we obtain $\Delta \sim 0.88$ eV at zero field.

While it increases with increasing temperature (not shown), the figure of merit ZT = $S^2T/\kappa\rho$ is very low, reaching ~4E-8 at 400 K. As mentioned previously, this is due to high resistivity. According to first principles calculations, $FeMn_2O_4$ is expected to be half metallic [5]. Whether this is true requires further study, as it is related to the degree of inversion in spinel materials [5]. One way to improve the thermoelectric properties of $FeMn_2O_4$ is to introduce chemical doping for suppressing magnetic interaction and increasing the concentration of charge carriers so to further lower down thermal conductivity and electrical resistivity. Of course, this requires the retention of the spinel structure.

SUMMARY

In summary, we have investigated the structural, magnetic, thermal, and electrical properties of single crystal $FeMn_2O_4$ in a wide temperature range, mostly for the first time. Three phase transitions are identified. One is the structural transition at $T_s \sim 595$ K from cubic at high temperatures to tetragonal (also called pseudo-cubic) at low temperatures through neutron powder diffraction measurement. Other two are magnetic transitions at $T_{FI\text{-}1} \sim 373$ K and $T_{FI\text{-}2} \sim 50$ K, respectively. Due to negative asymptotic Curie temperature extracted above $T_{FI\text{-}1}$ and magnetic hysteresis loops below $T_{FI\text{-}1}$, the transition at $T_{FI\text{-}1}$ is considered as a ferrimagnetic magnetic ordering with anomaly reflected in the magnetization, specific heat, and thermopower. The reduction of the magnetization and wider hysteresis loops indicate the spin rearrangement below $T_{FI\text{-}2}$. However, no anomaly is clearly seen in both thermal conductivity and specific heat, suggesting little entropy removal for the low-temperature spin configuration. Remarkably, the low-temperature specific heat and thermal conductivity are mostly carried by magnetic excitation, giving rise to $T^{3/2}e^{-\Delta_m/T}$ dependence. This strongly suggests that phonons in this crystalline system conduct little heat particularly at low temperatures. Such characteristic is promising for thermoelectric application. However, much better electrical conduction is required, as it is currently insulating with energy gap of 0.88 eV.

Acknowledgments

This material is based upon work supported by the U.S. Department of Energy under EPSCoR Grants No. DE-SC0016315 (RN, SD, RJ) and No. DE-SC0012432 with additional support from the Louisiana Board of Regents (QZ). This research used resources at the High Flux Isotope Reactor, a DOE Office of Science User Facility operated by the Oak Ridge National Laboratory. S. N. and W. T. were supported by the Scientific User Facilities Division, Basic Energy Sciences, U. S. DOE.

References

[1] V. W. J. Verhoeven, F. M. Mulder, and I. M. De Schepper, Phys. B Condens. Matter **276–278**, 950 (2000).

[2] V. Kocsis, S. Bordács, D. Varjas, K. Penc, A. Abouelsayed, C. A. Kuntscher, K. Ohgushi, Y. Tokura, and I. Kézsmárki, Phys. Rev. B **87**, 64416 (2013).

[3] V. Fritsch, J. Hemberger, N. Büttgen, E.-W. Scheidt, H.-A. Krug von Nidda, A. Loidl, and V. Tsurkan, Phys. Rev. Lett. **92**, 116401 (2004).

[4] R. Fichtl, V. Tsurkan, P. Lunkenheimer, J. Hemberger, V. Fritsch, H.-A. K. von Nidda, E.-W. Scheidt, and A. Loidl, Phys. Rev. Lett. **94**, 27601 (2005).

[5] D. Santos-Carballal, A. Roldan, R. Grau-Crespo, and N. H. de Leeuw, Phys. Rev. B **91**, 195106 (2015).

[6] U. Lüders, A. Barthélémy, M. Bibes, K. Bouzehouane, S. Fusil, E. Jacquet, J.-P. Contour, J.-F. Bobo, J. Fontcuberta, and A. Fert, Adv. Mater. **18**, 1733 (2006).

[7] K. E. Sickafus, J. M. Wills, and N. W. Grimes, J. Am. Ceram. Soc. **82**, 3279 (2004).

[8] A. Elfalaky and S. Soliman, J. Alloys Compd. **580**, 401 (2013).

[9] M. L. Néel, Ann. Phys. (Paris). **12**, 137 (1948).

[10] D. S. Mathew and R.-S. Juang, Chem. Eng. J. **129**, 51 (2007).

[11] R. Buhl, J. Phys. Chem. Solids **30**, 805 (1969).

[12] V. A. M. Brabers, Phys. Status Solidi **33**, 563 (1969).

[13] P. J. Wojtowicz, Phys. Rev. **116**, 32 (1959).

[14] G. I. Finch, A. P. B. Sinha, and K. P. Sinha, Proc. R. Soc. London A Math. Phys. Eng. Sci. **242**, (1957).

[15] B. Boucher, R. Buhl, and M. Perrin, J. Appl. Phys. **40**, 1126 (1969).

[16] A. H. Morrish and IEEE Magnetics Society., *The Physical Principles of Magnetism* (IEEE Press, 2001).

[17] S. E. Harrison, C. J. Kriessman, and S. R. Pollack, Phys. Rev. **110**, 844 (1958).

[18] V. A. M. Brabers, J. Cryst. Growth **8**, 26 (1971).

[19] V. A. M. Brabers, J. Phys. Chem. Solids **32**, 2181 (1971).

[20] K. Naito, H. Inaba, and H. Yagi, J. Solid State Chem. **36**, 28 (1981).

[21] M. O'keeffe, J. Phys. Chem. Solids **21**, 172 (1961).

[22] S. C. Tarantino, M. Giannini, M. A. Carpenter, and M. Zema, IUCrJ **3**, 354 (2016).

[23] G. Srinivasan and M. S. Seehra, Phys. Rev. B **28**, 1 (1983).

[24] S. Nayak, S. Thota, D. C. Joshi, M. Krautz, A. Waske, A. Behler, J. Eckert, T. Sarkar, M.

S. Andersson, R. Mathieu, V. Narang, and M. S. Seehra, Phys. Rev. B **92**, 214434 (2015).

[25] C. Lacroix, P. Mendels, and F. Mila, *Introduction to Frustrated Magnetism Materials, Experiments, Theory* (Springer Berlin, 2013).

[26] R. N. Bhowmik, R. Ranganathan, and R. Nagarajan, Phys. Rev. B **73**, 144413 (2006).

[27] S. Thota and M. S. Seehra, J. Appl. Phys. **118**, 129901 (2015).

[28] M. Tanaka, T. Mizoguchi, and Y. Aiyama, J. Phys. Soc. Japan **18**, 1091 (1963).

[29] H. J. Lee, G. Kim, D. H. Kim, J.-S. Kang, C. L. Zhang, S.-W. Cheong, J. H. Shim, S. Lee, H. Lee, J.-Y. Kim, B. H. Kim, and B. I. Min, J. Phys. Condens. Matter **20**, 295203 (2008).

[30] V. O. Garlea, R. Jin, D. Mandrus, B. Roessli, Q. Huang, M. Miller, A. J. Schultz, and S. E. Nagler, Phys. Rev. Lett. **100**, 1 (2008).

[31] Q. Zhang, K. Singh, F. Guillou, C. Simon, Y. Breard, V. Caignaert, and V. Hardy, Phys. Rev. B **85**, 54405 (2012).

[32] E. S. R. Gopal, *Specific Heats at Low Temp.* (Plenum Press, New York, 1966), pp. 84–111.

[33] R. A. Fisher, F. Bouquet, N. E. Phillips, J. P. Franck, G. Zhang, J. E. Gordon, and C. Marcenat, Phys. Rev. B **64**, 134425 (2001).

[34] D. Villuendas, T. Tsutaoka, and J. M. Hernàndez Ferràs, J. Magn. Magn. Mater. **405**, 282 (2016).

[35] G. Balaji, N. . S. Gajbhiye, G. Wilde, and J. Weissmüller, J. Magn. Magn. Mater. **242–245**, 617 (2002).

[36] K. P. Sinha and U. N. Upadhyaya, Phys. Rev. **127**, 432 (1962).

[37] G. S. Dixon, Phys. Rev. B **21**, 2851 (1980).

[38] C. Kittel, *Introduction to Solid State Physics* (Wiley, 2005).

[39] R. Jin, Y. Onose, Y. Tokura, D. Mandrus, P. Dai, and B. C. Sales, Phys. Rev. Lett. **91**, 146601 (2003).

[40] V. A. M. Brabers, Y. G. Proykova, N. Salerno, and T. E. Whall, J. Appl. Phys. **61**, 4390 (1987).

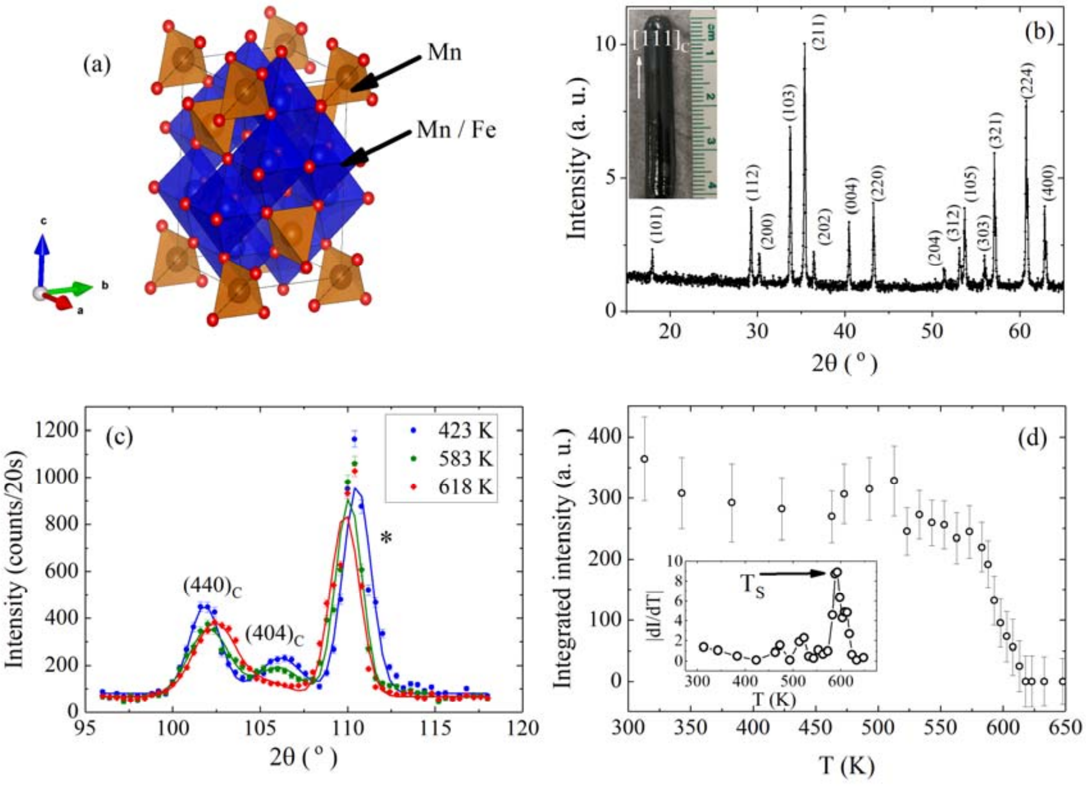

FIG. 1. (a) Crystal structure of FeMn$_2$O$_4$; (b) Powder x-ray diffraction pattern at room temperature with all peaks indexed in the *I41/amd* tetragonal symmetry. Inset: an as-grown single crystal with the growth direction indicated by an arrow; (c) (440)$_C$ and (404)$_C$ nuclear peaks indexed in pseudo-cubic notation at indicated temperatures via neutron powder diffraction measurements. The peak indicated by * is the aluminum (220) peak from the Al sample holder; (d) Temperature dependence of the integrated intensity of (404)$_C$ nuclear peak. Inset: the derivative of the (404)$_C$ peak intensity for T$_s$ determination.

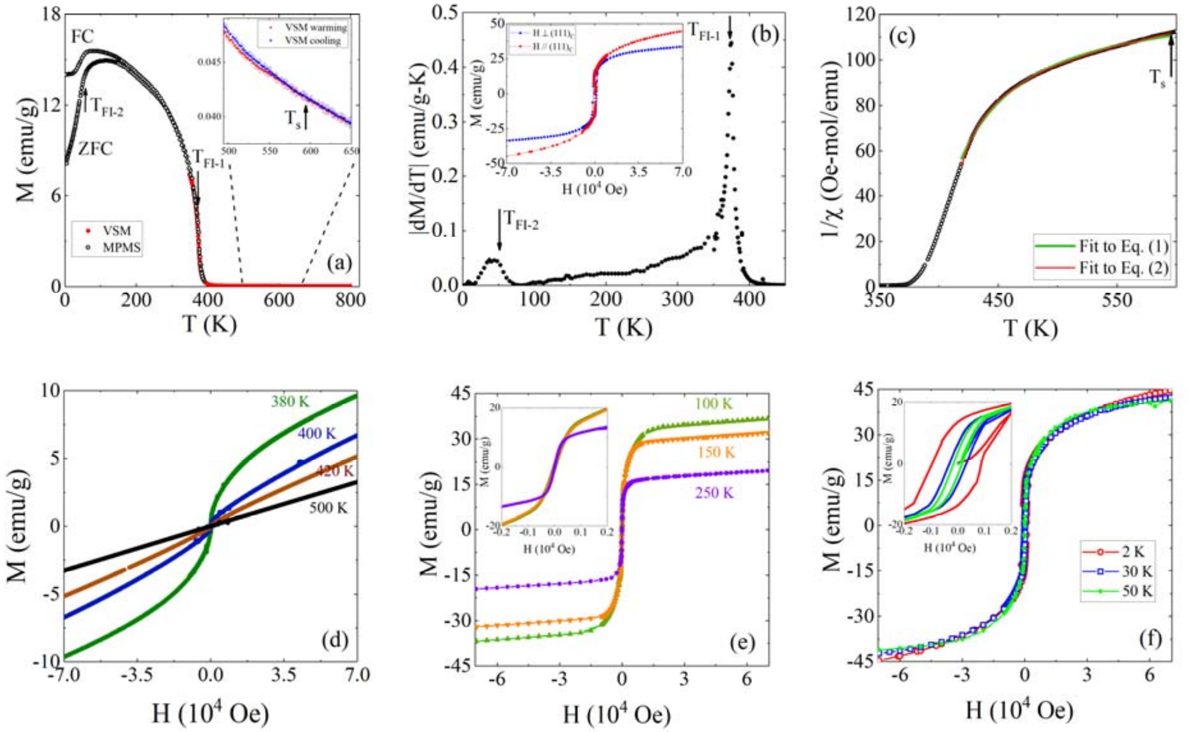

FIG. 2. (a) Temperature dependence of the magnetization (M) under H = 1 kOe. Inset: zoomed in view of M near T_s; (b) Derivative of M with respect to temperature for the determination of T_{FI-1} and T_{FI-2}; Inset: Field dependence of magnetization at 2 K with magnetic field parallel to $(111)_C$ (red) and perpendicular to $(111)_C$ (blue). (c) Inverse magnetic susceptibility as a function of temperature; (d), (e), and (f) Isothermal magnetization hysteresis loops at indicated temperatures with $T > T_{FI-1}$, $T_{FI-1} > T > T_{FI-2}$, and $T < T_{FI-2}$, respectively. Insets of (e) and (f): zoomed in view of M(H) from -2 kOe to 2 kOe.

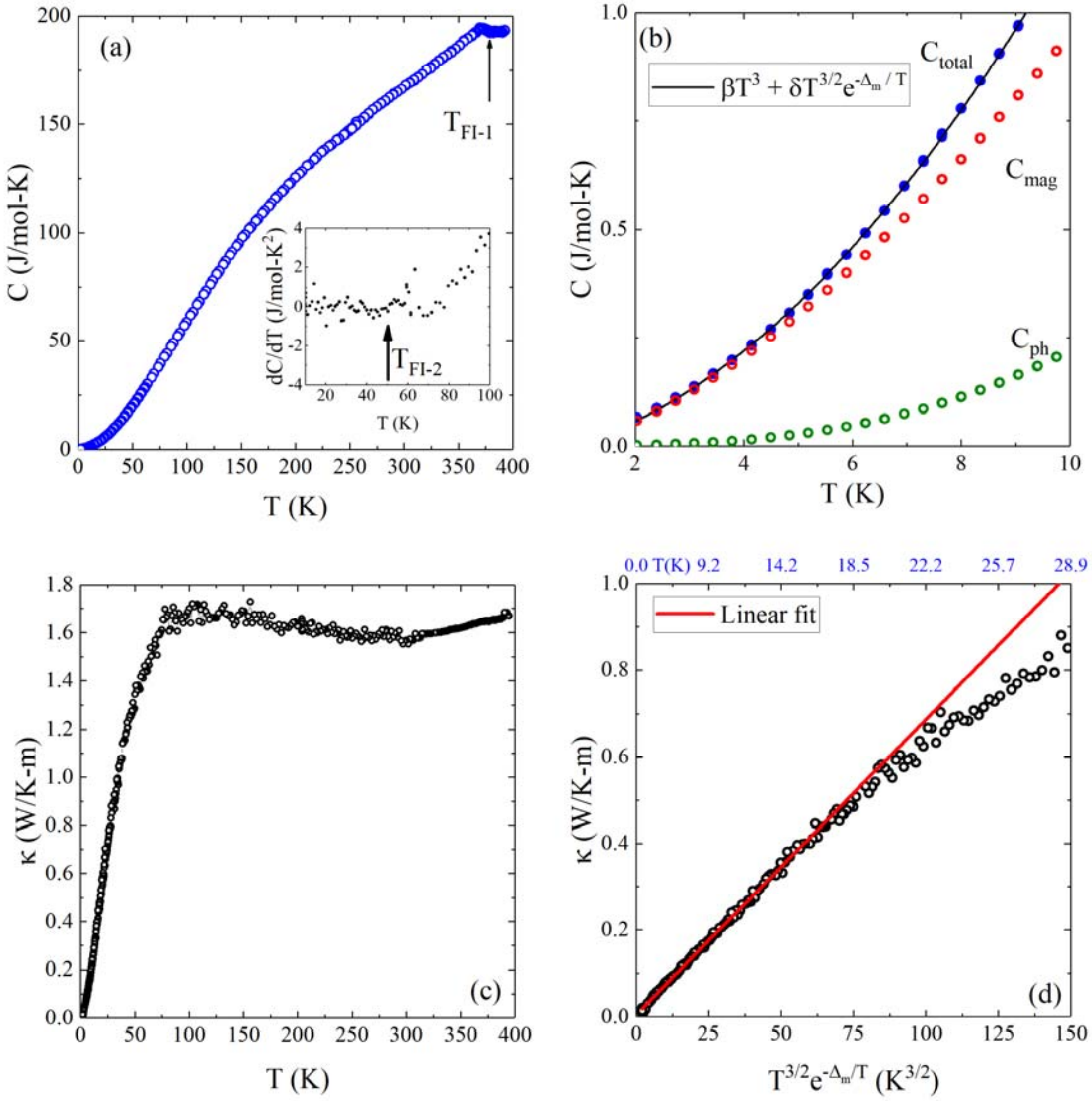

FIG. 3. (a) Temperature dependence of the specific heat (C_p). Inset: derivative of C_p near $T_{FI\text{-}2}$; (b) Low-temperature C_p with the fitting curve using Eq. (3) i.e. $\beta T^3 + \delta T^{3/2} e^{-\Delta_m/T}$. Both C_{ph} and C_{mag} are presented; (c) Temperature dependence of thermal conductivity (κ); (d) Low-temperature κ plotted as a function of $T^{3/2} e^{-\Delta_m/T}$. The solid line is the fitting line (see text).

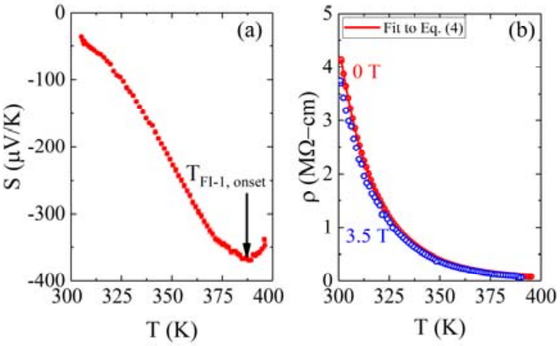

FIG. 4. (a) Temperature dependence of the thermopower (S), where T_{FI-1} onset is indicated; (b) Electrical resistivity (ρ) as a function of temperature at H = 0 and 3.5 Tesla. The solid curve is the fit of data to Eq. (4).